A theory for how the depth of meltwater injection impacts regional sea level evolution

Aurora Basinski-Ferris[a] , Laure Zanna[a] , and Ian Eisenman[b]

[a] *Courant Institute of Mathematical Sciences, New York University, New York, NY, USA*

[b] *Scripps Institution of Oceanography, University of California San Diego, La Jolla, CA, USA*

Corresponding author: Aurora Basinski-Ferris, abf376@nyu.edu

Early Online Release: This preliminary version has been accepted for publication in *Journal of Physical Oceanography*, may be fully cited, and has been assigned DOI 10.1175/JPO-D-24-0153.1. The final typeset copyedited article will replace the EOR at the above DOI when it is published.

ABSTRACT: Mass loss from the Antarctic ice sheet is projected to continue over the coming century. The resultant sea level change will have a regional pattern that evolves over time as the ocean adjusts. Accurate estimation of this evolution is crucial for local communities. Current state-of-the-art climate models typically do not couple ice sheets to the atmosphere-ocean system, and the impact of ice sheet melt has often been studied by injecting meltwater at the model ocean surface. However, observational evidence suggests that most Antarctic meltwater enters the ocean at depth through ice shelf basal melt. A previous study has demonstrated that the regional sea level pattern at a given time depends on meltwater injection depth. Here, we introduce a 2.5-layer model to investigate this dependence and develop a theory for the associated adjustment mechanisms. We find mechanisms consistent with previous literature on the ocean adjustment to changes in forcing, whereby a slower Rossby wave response off the eastern boundary follows a fast response from the western boundary current and Kelvin waves. We demonstrate that faster baroclinic Rossby waves near the surface than at depth explains the injection depth dependence of the adjustment in the 2.5-layer model. The identified Rossby wave mechanism may contribute to the dependence of the ocean's transient adjustment on meltwater injection depth in more complex models. This work highlights processes that could cause errors in the projection of the time-varying pattern of sea level rise using surface meltwater input to represent Antarctica's freshwater forcing.

SIGNIFICANCE STATEMENT: Sea level rise is expected to be larger in some locations than others. Accurate projections of the pattern of sea level change, which changes in time as the ocean adjusts, is essential information for local communities. One of the factors that leads to uncertainty in the local sea level change due to Antarctic melt is the depth at which this meltwater is input into an ocean model. We propose a mechanism for a faster response of sea level around the basin when meltwater is injected at the ocean surface compared to when it is injected well below the surface. This mechanism has implications for projections of the regional sea level response to Antarctic melt.

1. Introduction

During recent decades, Antarctica has been losing mass, which has caused a global mean sea level increase from 1992 to 2020 of 7.4 ± 1.5 millimeters (Otosaka et al. 2023). Projections indicate continued Antarctic mass loss, likely raising global mean sea level by up to 28cm by 2100 and driving an accelerated rise into the 22nd century (Oppenheimer et al. 2019). In particular, West Antarctica, which is the location of the most mass loss on the Antarctic ice sheet (Adusumilli et al. 2020), has a capacity to raise global mean sea level by 5.3m if the ice completely melts (Morlighem et al. 2020, Table S3). However, contributions to sea level rise, such as from ice sheets, glaciers, and steric changes, are not globally uniform (e.g., Kopp et al. 2015; Hamlington et al. 2020; Todd et al. 2020). For adaptation efforts, projecting the time-evolving pattern of regional sea level change is particularly crucial. In the case of sea level rise from ice sheet melt, regional variation in sea level will be determined by changes in Earth's gravitation, rotation, and deformation (e.g., Farrell and Clark 1976; Kopp et al. 2010; Mitrovica et al. 2018), as well as ocean dynamic processes which propagate and are affected by the meltwater injection (e.g., Stammer 2008; Lorbacher et al. 2012; Kopp et al. 2010; Schmidt et al. 2023).

The largest contributor to Antarctic mass loss is the basal melt of ice shelves (Pritchard et al. 2012; Rignot et al. 2013; Depoorter et al. 2013). Observations near west Antarctic ice shelves indicate that this meltwater settles at depth after exiting the ice shelf cavity (Kim et al. 2016; Garabato et al. 2017), likely due to turbulent mixing processes between the meltwater plume and the rest of the water column (Garabato et al. 2017). However, full complexity atmosphere-ocean models, including those in the CMIP5 and CMIP6 ensembles, are not currently coupled to ice sheet models (Taylor et al. 2012; Eyring et al. 2016), although there has been recent work in this direction (Smith et al. 2021). Thus, climate projections with meltwater forcing included are typically performed by prescribing a freshwater input, which is often added to the surface net precipitation field, known as “hosing experiments” (e.g., Stammer 2008; Lorbacher et al. 2012; Kopp et al. 2010; Bronselaer et al. 2018; Golledge et al. 2019; Moorman et al. 2020; Li et al. 2023b; Schmidt et al. 2023; Park et al. 2023). This discrepancy between the vertical distribution of meltwater in observations and the typical approach in modelling studies motivated a previous study which demonstrated in a simplified single basin model that an idealized representation of Antarctic meltwater injected at depth adjusts the dynamic sea level more slowly across the basin than meltwater injected at the surface (Eisenman et al. 2024). This sensitivity to vertical meltwater distribution falls under a broad category of potential sensitivities of the ocean response to choices in meltwater hosing experiments, which have been identified as targets for community investigation (Swart et al. 2023).

Here, we focus on the baroclinic response of sea level to meltwater input, which largely determines the dynamic sea level pattern, and occurs after a spatially uniform and rapid barotropic response (Eisenman et al. 2024). We present a simplified model and develop a theory to explore the difference in this baroclinic adjustment when inputting a volume anomaly at depth compared to at the surface, which ultimately leads to a different sea level pattern at a given time. We utilize a reduced gravity model, which is a class of models that is used for simplified representations of the upper ocean. For example, reduced gravity models have been utilized in simple models of El Niño (e.g., Cane and Zebiak 1985; Chang et al. 2006; Guo et al. 2022) and to understand adjustment to changes in deep water formation (e.g., Kawase 1987; Huang et al. 2000; Johnson and Marshall 2002, 2004; Cessi et al. 2004; Zhai et al. 2011; Nieves and Spall 2018; Sun et al. 2020), North Atlantic or Southern Ocean heat sources (Hsieh and Bryan 1996), and changes in wind stress (e.g., Cessi and Otheguy 2003; Zhai et al. 2014). In the present work, we examine the large scale dynamical adjustment to volume input at the southern end of a rectangular domain utilizing a reduced gravity model with two active layers (2.5-layer model). Much of the theory developed is analogous to previous studies of other phenomena (e.g., Johnson and Marshall 2002), but we include an additional active layer, to investigate the vertical dependence of the adjustment processes.

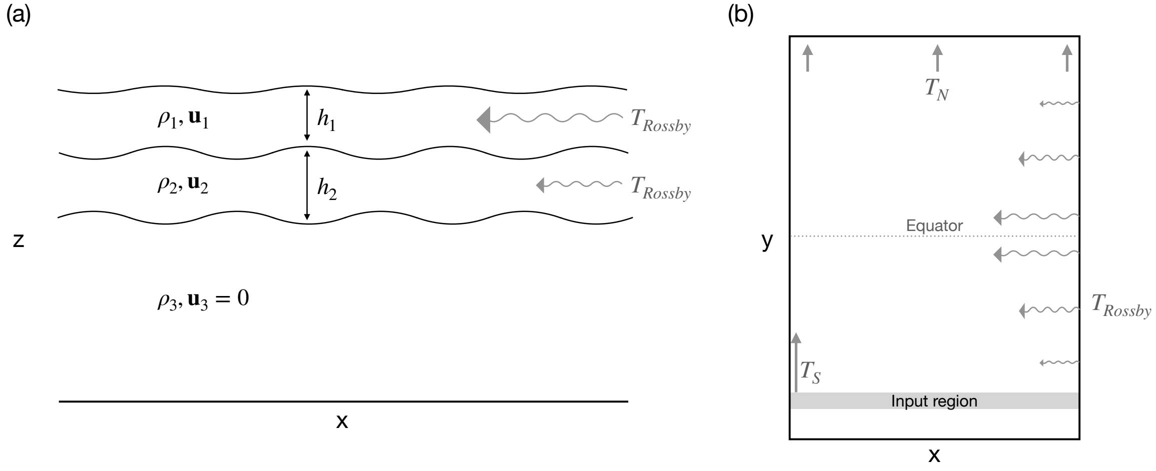

FIG. 1. Adjustment mechanism schematic in 2.5-layer reduced gravity model. (a) model set-up in longitude and depth space. The top two layers are active with unconstrained $\mathbf{u_i}$, while the abyssal (third) layer is motionless. We highlight the essential mechanism of adjustment (see Section 3), whereby a top-layer volume perturbation propagates an upper ocean anomaly faster than a bottom-layer perturbation due to faster baroclinic Rossby waves. (b) the domain in longitude and latitude space with a schematic of the adjustment mechanism. In both panels, the notation T_{Rossby} is used as in Johnson and Marshall (2002) and indicates volume fluxes due to Rossby waves.

This paper is organized as follows: in Section 2, we introduce the 2.5-layer model and compare this idealized model to the results in Eisenman et al. (2024). We present an analytic theory for the ocean's dynamical response to meltwater input in Section 3, highlighting the essential physical processes that lead to faster transport of a meltwater perturbation near the surface compared to at depth. In Section 4, we discuss the sensitivity of the results to parameter choices and the potential effect of Ekman transport. We conclude in Section 5.

2. Dynamic adjustment to meltwater input in a hierarchy of numerical simulations

As presented in Eisenman et al. (2024) using runs in MITgcm, the adjustment of dynamic sea level throughout a single basin is slower for idealized Antarctic meltwater perturbations injected at depth than for perturbations injected at the surface. In particular, this difference in adjustment was attributed to the different timescales associated with the baroclinic (largely steric) response of the ocean (following rapid barotropic waves, which have a largely globally uniform imprint). Here, we introduce a simplified model, designed to capture baroclinic processes, to investigate the adjustment mechanisms and the difference in propagation of anomalies input at depth compared to at the surface.

a. 2.5-layer model set-up

We define a 2.5-layer reduced gravity model consisting of 2 active layers with densities ρ_1 and ρ_2 on top of a quiescent abyss with density ρ_3. The abyss is a layer of no motion and, thus, has horizontally uniform pressure. The model is defined with linearized momentum equations and non-linear continuity equations:

$$\frac{\partial \mathbf{u_i}}{\partial t} + \mathbf{f} \times \mathbf{u_i} = -\delta_{i,1} g_1' \nabla h_1 - g_2' \nabla (h_1 + h_2) + \nu \nabla^2 \mathbf{u_i} - r \mathbf{u_i}, \tag{1}$$

$$\frac{D h_i}{D t} + h_i \nabla \cdot \mathbf{u_i} = S_i(x, y), \tag{2}$$

where $\delta_{i,1}$ is a Kronecker delta. Here, h_i is the layer thickness in the i^{th} layer with $i = 1, 2$, $\mathbf{u}_i = (u_i, v_i)$ is the velocity vector, ∇ is the two-dimensional gradient operator, $g_i' = g\frac{\rho_{i+1} - \rho_i}{\rho_0}$ is the i^{th} reduced gravity with ρ_0 the reference density, $\frac{D}{Dt} = \left(\frac{\partial}{\partial t} + \mathbf{u} \cdot \nabla\right)$ is the material derivative, and ν is the viscosity coefficient set to $\nu = 8 \times 10^3$ m^{2}s^{-1}. The Rayleigh friction term is only active in the sponge layers (see Figure 2) which are described in detail in Appendix A. Imposed sources and sinks in the domain in layer i are denoted as $S_i(x, y)$, while initial layer thicknesses prior to the introduction of sources or sinks will be denoted H_i. A schematic of the model is shown in Figure 1a. The domain size is chosen to have the same surface area as that of the MITgcm set-up that we compare against; however, the domains have different shapes because the 2.5-layer model is run in a rectangular domain on a Cartesian grid, whereas MITgcm is run on a latitude-longitude grid. Details for the numerical solution of the 2.5-layer model are given in Appendix A.

We test the sensitivity of adjustment mechanisms to a zonal wind forcing in the southern part of the domain in the 2.5-layer model simulations by modifying Equation (1) such that:

$$\frac{\partial \mathbf{u_i}}{\partial t} + \mathbf{f} \times \mathbf{u_i} = -\delta_{i,1} g_1' \nabla h_1 - g_2' \nabla (h_1 + h_2) + \nu \nabla^2 \mathbf{u_i} - r \mathbf{u_i} + \delta_{i,1} \frac{\boldsymbol{\tau}}{\rho_1 H_1}, \tag{3}$$

where $\boldsymbol{\tau} = (\tau(y,t), 0)$ is the imposed zonal wind forcing.

In this work, we focus on two types of perturbation experiments, designed as simplified representations of Antarctic meltwater input at different depths (see Figure 2): volume additions into (1) the top active layer ($i = 1$) and (2) the bottom active layer ($i = 2$).

b. Upper ocean response in MITgcm and the 2.5-layer model

In a Boussinesq ocean model, such as MITgcm, the free surface evolves due to volume convergence which may occur due to transport processes at any depth. Here, we focus on the upper ocean thickness, which is reflective of the transport in the upper ocean. We determine the upper ocean thickness, $h_u(x,y,t)$, as the thickness above a given isopycnal that correlates to the upper ocean in the control state (located at approximately 1000m depth, see Figure B1):

$$h_u(x,y,t) = \sum_1^n h_i(x,y,t), \tag{4}$$

where h_i is the thickness associated with the ith isopycnal layer and n is the layer chosen to sum up to; here, potential density increases with increasing layer number. The h_i layers adjust due to convergence of volume within the layers (in a Boussinesq model, this includes mixing processes). In the 2.5-layer model presented in this paper, a comparable metric of the upper ocean thickness is the sum of the thickness of the active layers ($h_1 + h_2$), which are representing the upper ocean.

In Figure 3, we focus on this upper ocean thickness metric in both models. In particular, we examine the Northern Hemisphere upper ocean thickness anomaly, which is the Northern Hemisphere mean upper ocean thickness minus the global mean upper ocean thickness. We focus on the Northern Hemisphere anomaly, as this is indicative of the response at the *opposite* end of the basin from the meltwater input, and thus summarizes the adjustment throughout the basin. Comparable plots would be equal and opposite for the Southern Hemisphere anomaly, when averaging over the whole domain (i.e., not just the analytic region).

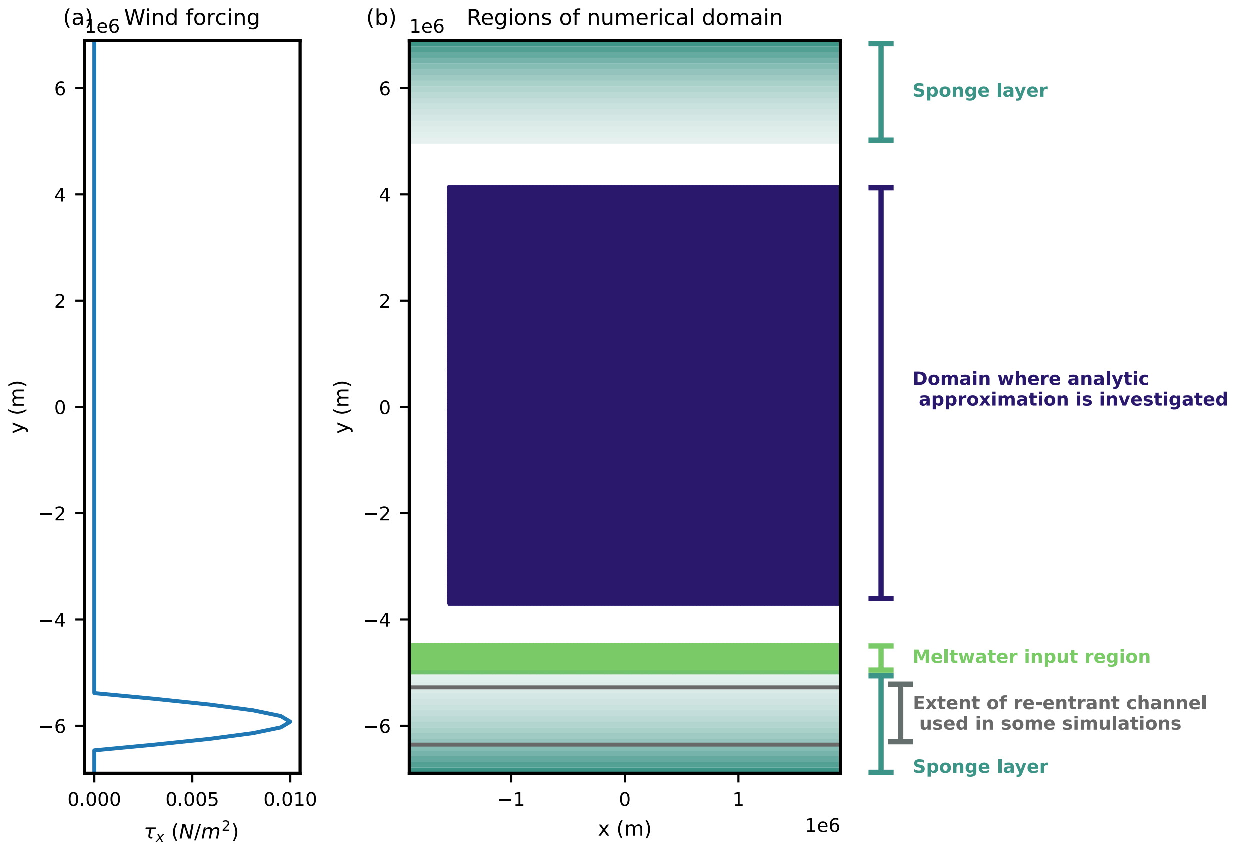

Fig. 2. (a): Wind forcing profile; (b) Diagram showing domain regions used for the 2.5-layer reduced gravity model. The extent of the sponge layers is defined as regions where *any* Rayleigh damping is present. Note that the strength of the damping decays exponentially away from the north/south walls, as illustrated in the diagram, although the visual representation of this decay is less strong than in the numerical solution. In purple, we denote the region where we solve for the theoretical solution in Section 3 (analytic domain); the meltwater input region (green) is at the southern edge of the analytic domain. The analytic region excludes the western boundary current region and a few grid cells near the sponge layers in order to focus on: (1) the dynamics in the interior, and (2) the region unaffected by numerical effects from the sponge layers. The re-entrant channel region is shown, but it is only utilized in experiments where wind is applied. Note that the re-entrant channel is within the sponge layer, but is located where the damping is sufficiently weak to allow Ekman transport to be driven.

Figure 3a shows the Northern Hemisphere upper ocean thickness anomaly, scaled by the total thickness change around the first equilibration of the deep perturbation (at year 110 after meltwater introduction) in the simulations presented in Eisenman et al. (2024). The faster adjustment of

Northern Hemisphere sea level in experiments with meltwater anomalies input at the surface compared to anomalies input at depth is driven by the upper ocean thickness, as we capture the faster adjustment in this metric. Thus, the upper ocean processes are key to explaining the result in Eisenman et al. (2024), which demonstrated faster propagation of steric anomalies away from the input region in a surface perturbation experiment compared to a deep perturbation experiment.

Figure 3b and c presents results for the adjustment of volume perturbations in the 2.5-layer model, which are introduced when the ocean is at rest such that the meltwater perturbation itself induces all transport. We choose $g_1' = g_2' = g\frac{2}{1026}$ and initial layer thicknesses $H_1 = H_2 = 250$m as physically reasonable upper ocean parameter choices (see Section 4a for the sensitivity to parameters). We input a volume perturbation via a step function of 0.1 Sv into the input region of either layer 1 or 2, as indicated in Figure 2b. Figure 3b shows the Northern Hemisphere upper ocean scaled thickness anomaly, which is normalized by the equilibrated total thickness anomaly (year 41 after meltwater input), such that this quantity is directly comparable to Figure 3a. As in MITgcm, we find that the upper ocean thickness adjusts more quickly in the Northern Hemisphere due to a top-layer perturbation than a bottom-layer perturbation (Figure 3b). We include an analytic estimate (dashed lines), developed in Section 3, by taking the Northern Hemisphere mean over the purple region in Figure 2; see Appendix A for a small quantitative difference in the numerical result averaged over the entire domain. In Figure 3a and b, we have scaled by the global mean change for the best comparison between models because the global mean upper ocean thickness changes entirely due to meltwater input in the 2.5-layer model, but is larger in the MITgcm simulations because mixing processes also affect the volume. Figure 3c is comparable to Figure 3b, but without scaling by the global mean thickness change.

The 2.5-layer model has a small sea level change which is not equivalent to the upper ocean thickness metric chosen here (see Appendix B2). However, we find that the initial result presented in Eisenman et al. (2024), which demonstrated faster adjustment of dynamic sea level throughout the basin in a surface perturbation experiment compared to a deep perturbation experiment, is driven by the adjustment of the upper ocean. Thus, we focus on this upper ocean adjustment, and we develop a theory which can explain key mechanisms and their associated relative timescales in the simplified model.

3. An analytical theory for adjustment

We aim to develop an analytical theory for the dynamical response to volume input near the southern edge of the 2.5-layer model. We assume that adjustment mechanisms similar to other reduced gravity model studies will prevail (e.g., Kawase 1987; Hsieh and Bryan 1996; Huang et al. 2000; Johnson and Marshall 2002, 2004; Cessi et al. 2004; Zhai et al. 2011; Nieves and Spall 2018), but we consider the processes with an additional active layer compared to these previous studies. That is, we assume that the height perturbation is first propagated by a fast response such that: (1) the volume anomaly induces a transport along the western boundary, which propagates some volume northward, toward the equator; (2) the volume anomaly travels across the equator as a Kelvin wave; (3) the volume anomaly travels along the eastern boundary as Kelvin waves, resulting in near uniform height along the boundary. The height anomaly's slower propagation into the basin's interior is then governed by baroclinic Rossby waves emanating from the eastern boundary. As we are interested in the multidecadal to centennial adjustment, we view the three fast mechanisms above as occurring instantaneously, and we aim to develop an analytic theory to explain the relatively slow adjustment driven by the propagation of baroclinic Rossby waves. In particular, we aim for the theory developed to highlight the vertical dependence of the processes which adjust the upper ocean thickness anomaly throughout the basin (here indicated by the Northern Hemisphere anomaly, see Figure 3).

a. Assumptions and preliminaries

We approximate that the relevant dynamics for volume adjustment in the interior of the basin on multidecadal to centennial timescales are captured by geostrophic balance

$$f\mathbf{u}_i = \mathbf{k}\times\nabla\left(g_2'(h_1+h_2)+\delta_{i,1}g_1'h_1\right), \tag{5}$$

and the continuity equations linearized around the starting layer thicknesses (H_i) with no source or sink terms

$$\frac{\partial h_i}{\partial t}+H_i\nabla\cdot\mathbf{u_i}=0, \tag{6}$$

for layers $i = 1,2$. In Equation (5), the Rayleigh damping term is absent, since it is only active in the sponge layers. We have, however, assumed that the viscous term can be neglected in the interior (although it is an important term in the western boundary current region to close the basin's circulation). We obtain evolution equations for the interior layer thicknesses by combining Equations (5) and (6):

$$\frac{\partial h_i}{\partial t} + \frac{H_i \beta g_2'}{f^2} \frac{\partial (h_1 + h_2)}{\partial x} + \delta_{i,1} \frac{H_1 \beta g_1'}{f^2} \frac{\partial h_1}{\partial x} = 0, \tag{7}$$

with $i = 1,2$ and $\beta \equiv \frac{df}{dy}\big|_\theta$ evaluated at a given latitude θ. Here, we will utilize a beta plane approximation centered at the equator, and thus $\beta \simeq 2.20 \times 10^{-11} \mathrm{m}^{-1} \mathrm{s}^{-1}$. The advection equations (Equation 7) differ between the two active layers of the model due to the representation of geostrophic balance, which includes an additional term in the top-layer ($i = 1$). This layer-wise difference in the geostrophic velocities corresponds to the model's thermal wind relation.

b. Rossby wave adjustment off the eastern boundary

To capture the multidecadal adjustment, we proceed by solving Equation (7). For simplicity, we use that $H \equiv H_1 = H_2$ and $g_1' = g_2'$ and denote $c(y) = \frac{\beta g_2'}{f^2} = \frac{\beta g_1'}{f^2}$. (In Appendix D1, we relax these assumptions and present a general solution). We rewrite the coupled advection system given by Equation (7) for both layers as:

$$\frac{\partial \mathbf{h}}{dt} + \mathbf{A} \cdot \frac{\partial \mathbf{h}}{dx} = 0, \tag{8}$$

with $\mathbf{h}(x,y,t) = [h_1(x,y,t), h_2(x,y,t)]$ and

$$\mathbf{A} = Hc(y) \begin{bmatrix} 2 & 1 \\ 1 & 1 \end{bmatrix}. \tag{9}$$

We diagonalize the matrix $\mathbf{A} = \mathbf{P}^{-1} \mathbf{\Lambda} \mathbf{P}$ to decouple the equations in a new set of variables $\mathbf{w}(x,y,t) = [w_1, w_2] = \mathbf{Ph}$. The decoupled linear advection equations in the variable $\mathbf{w}$ are given by

$$\frac{\partial \mathbf{w}}{dt} + \mathbf{\Lambda} \frac{\partial \mathbf{w}}{dx} = 0, \tag{10}$$

where the entries of $\mathbf{\Lambda} = (\lambda_1, \lambda_2)$ are the eigenvalues of $\mathbf{A}$, $\lambda_1(y) = \frac{3+\sqrt{5}}{2}Hc(y)$ and $\lambda_2(y) = \frac{3-\sqrt{5}}{2}Hc(y)$. The solution for each variable is given using the method of characteristics such that

$$w_i(x,y,t) = w_i(x - \lambda_i(y)t, y, 0), \tag{11}$$

for $i = 1,2$. Equation (11) indicates that information shifts (westward) at the speed given by the eigenvalue. Given our hypothesized mechanism, which has the eastern boundary approximately equilibrated through the fast response, we interpret Equation (11) as a set of delay equations off the eastern boundary. We perform a transformation back to **h** coordinates and write the variables explicitly in terms of the eastern boundary timeseries:

$$h_1(x,y,t) = \underbrace{\alpha_+ h_1(x_e, t - \tfrac{L_x - x}{\lambda_1(y)})}_{i} + \underbrace{\alpha_1 h_2(x_e, t - \tfrac{L_x - x}{\lambda_1(y)})}_{ii} + \underbrace{\alpha_2 h_1(x_e, t - \tfrac{L_x - x}{\lambda_2(y)})}_{iii} - \underbrace{\alpha_1 h_2(x_e, t - \tfrac{L_x - x}{\lambda_2(y)})}_{iv} \tag{12}$$

$$h_2(x,y,t) = \underbrace{\alpha_1 h_1(x_e, t - \tfrac{L_x - x}{\lambda_1(y)})}_{i} + \underbrace{\alpha_2 h_2(x_e, t - \tfrac{L_x - x}{\lambda_1(y)})}_{ii} - \underbrace{\alpha_1 h_1(x_e, t - \tfrac{L_x - x}{\lambda_2(y)})}_{iii} + \underbrace{\alpha_+ h_2(x_e, t - \tfrac{L_x - x}{\lambda_2(y)})}_{iv}, \tag{13}$$

where $\alpha_1 = \frac{1}{\sqrt{5}}$, $\alpha_2 = \frac{5-\sqrt{5}}{10}$, $\alpha_+ = \alpha_1 + \alpha_2$, x_e is the location of the eastern boundary, and L_x is the longitudinal extent of the domain. Any h_i terms evaluated at the eastern boundary no longer have latitudinal dependence because the assumed fast response sets the eastern boundary height regardless of y; thus, $h_i(x,y,t)$ terms evaluated at the eastern boundary are written as $h_i(x_e,t)$.

The faster height adjustment in the top layer than the bottom layer is evident through examining the lag terms in Equations (12) and (13). We focus first on lag terms off the eastern boundary height in layer i which affect $h_j(x,y,t)$ for $i = j$. For these terms, there is a larger coefficient on the fast timescale in the top layer equation than the bottom layer equation (compare term i in Equation (12) to term ii in Equation (13)); there is a corresponding larger coefficient on the slow timescale in the bottom layer equation than the top layer equation (compare term iii in Equation (12) to term iv in Equation (13)). The remaining terms, which are lag terms off the eastern boundary in layer i which affect $h_j(x,y,t)$ for $i \neq j$, have the same coefficients ($\pm\alpha_1$) and do not account for a difference in adjustment.

The timescales λ_1 and λ_2 are determined by the long baroclinic Rossby wave speeds associated with the baroclinic modes in the 2.5-layer model (see Appendix C). Thus, the coefficient differences noted above are equivalent to a larger projection of the faster mode onto the top layer than the bottom layer. This Rossby wave mechanism explains the faster propagation throughout the basin, visible in the upper ocean thickness adjustment, depending on the depth of the volume perturbation.

c. Time evolution of eastern boundary height

In Section 3b, we found an analytic solution for the propagation of information westward, which we are interpreting as governing interior upper ocean adjustment through lag equations off the eastern boundary height. Thus, we must also find the eastern boundary height timeseries, which we aim to relate to meridional fluxes in and out of the analytic domain. We will proceed with a general derivation without assuming equal thickness or reduced gravity between the two active layers, introducing $c_1(y) = \frac{\beta g_1'}{f^2}$ and $c_2(y) = \frac{\beta g_2'}{f^2}$.

We find the volume evolution at each latitude by zonally integrating Equation (7) from the eastern boundary (denoted x_e) to the edge of the western boundary current (denoted x_b), for each layer. We assume that the volume of the boundary region is small, i.e., that $\int_{x_w}^{x_e} h_i dx \approx \int_{x_b}^{x_e} h_i dx$, where x_w denotes the longitude of the western wall of the basin. Thus, the volume budget for each latitudinal band is:

$$\frac{\partial}{\partial t}\int_{x_w}^{x_e} h_1(x,y,t)dx = H_1c_2(y)\left[h_1(x_e,t) - h_1(x_b,y,t) + h_2(x_e,t) - h_2(x_b,y,t)\right] + H_1c_1(y)[h_1(x_e,t) - h_1(x_b,y,t)], \tag{14}$$

$$\frac{\partial}{\partial t}\int_{x_w}^{x_e} h_2(x,y,t)dx = H_2c_2(y)\left[h_1(x_e,t) - h_1(x_b,y,t) + h_2(x_e,t) - h_2(x_b,y,t)\right]. \tag{15}$$

As in Johnson and Marshall (2002), Equations (14) and (15) indicate that the layer thickness change at a given latitude depends on (zonal) volume fluxes. These fluxes propagate from the eastern boundary (terms of the form $H_ic_ih_i(x_e,t)$) and flow out of the interior of the basin at the western edge into the boundary current (terms of the form -$H_ic_ih_i(x_b,t)$).

We relate the volume evolution of each latitudinal band to meridional fluxes by zonally integrating the nonlinear continuity equations, using a no-normal flow condition at the walls, such that

$$\frac{\partial}{\partial t}\int_{x_w}^{x_e} h_i(x,y,t)dx = -\frac{\partial}{\partial y}T_i(y), \tag{16}$$

with $T_i(y) \equiv \int_{x_w}^{x_e} h_i v_i dx$ denoting the northward transport.

Thus, to find the full eastern boundary height, we can combine Equations (14), (15), and (16) and latitudinally integrate to write a volume budget for the analytic domain. This budget indicates that zonal fluxes (off the eastern boundary and eventually into the western boundary current) are equal to the difference in meridional fluxes at the southern and northern edges of the domain (denoted $T_{S,i}(t)$ and $T_{N,i}(t)$ respectively). The steps in this process are explicitly detailed in Appendix D2. Here, we show the final equations that can be solved for the eastern boundary heights in each layer as:

$$h_1(x_e,t)\int_0^{L_y} c_1(y)dy = \int_0^{L_y} c_1(y)h_1(x_b,y,t)dy + \frac{T_{S,1}(t)}{H_1} - \frac{T_{N,1}(t)}{H_1} - \frac{T_{S,2}(t)}{H_2} + \frac{T_{N,2}(t)}{H_2}, \quad (17)$$

$$\begin{aligned} h_2(x_e,t)\int_0^{L_y} c_2(y)dy = -h_{1,e}(t)\int_0^{L_y} c_2(y)dy + \int_0^{L_y} c_2(y)(h_1(x_b,y,t) + h_2(x_b,y,t))dy \\ + \frac{T_{S,2}}{H_2} - \frac{T_{N,2}}{H_2}. \end{aligned} \quad (18)$$

Equations (17) and (18) are solved iteratively together using that $h_i(x_b,y,t)$ is set by a time lag of $h_i(x_e,t)$ due to long baroclinic Rossby waves (see Equations (12) and (13)). In practice, we must avoid divergence of the integrals of $c_i(y)$ at the equator; here, we use that $H_i c_i(y) < 1$ (see Johnson and Marshall 2002). Taken together, Equations (17) and (18) can be fully solved given only northward fluxes at the north and south boundaries, which help set the eastern boundary heights; thus, these equations can be utilized to find the full adjustment of the interior h_i fields when combined with the theory in Section 3b. In the remainder of this subsection, we examine the meridional fluxes at the north and south boundaries (Section 3d) to complete the full analytical argument.

Accepted for publication in *Journal of Physical Oceanography*. DOI 10.1175/JPO-D-24-0153.1

d. Meridional fluxes at the edges of the domain

The meridional transport at a given latitude, including the north or south boundaries, can be found by using $T_i(y) \equiv \int_{x_w}^{x_e} h_i v_i dx$ and assuming geostrophic balance. Thus, at a given latitude (y):

$$T_1(y,t) = \frac{g_2' + g_1'}{2f}(h_1(x_e,t)^2 - h_1(x_w,y,t)^2) + \frac{g_2'}{f}\int_{x_w}^{x_e} \frac{dh_2}{dx} h_1 dx \tag{19}$$

$$T_2(y,t) = \frac{g_2'}{f}\int_{x_w}^{x_e} \frac{dh_1}{dx} h_2 dx + \frac{g_2'}{2f}(h_2(x_e,t)^2 - h_2(x_w,y,t)^2) \tag{20}$$

We simplify these expressions by noting that $\int_{x_w}^{x_e} \frac{dh_i}{dx} h_j dx \approx \int_{x_w}^{x_e} \frac{dh_i}{dx} h_i dx$ for $i \neq j$ as $h_i/h_j \approx 1$. For example, assessing this assumption numerically at the southern boundary, we find that the average deviation of $h_i/h_j (i \neq j)$ from 1 is 0.005 and the largest deviation at any location and time across both top and bottom perturbation experiments is 0.030.

Thus, we find the transport at both the northern and southern boundaries by using:

$$T_1(y,t) = \frac{g_2' + g_1'}{2f}(h_1(x_e,t)^2 - h_1(x_w,y,t)^2) + \frac{g_2'}{2f}(h_2(x_e,t)^2 - h_2(x_w,y,t)^2) \tag{21}$$

$$T_2(y,t) = \frac{g_2'}{2f}(h_1(x_e,t)^2 - h_1(x_w,y,t)^2 + h_2(x_e,t)^2 - h_2(x_w,y,t)^2) \tag{22}$$

The value of the eastern boundary is used as found from Equations (17) and (18), while the western boundary thicknesses are diagnosed from the model. We note that this is similar to how the solution is closed in the 1.5-layer model in Johnson and Marshall (2002), where the western boundary thickness is prescribed at the southern edge of the domain and the outflow is prescribed at the northern edge. Here, we do not prescribe values so as to allow the dynamics to freely evolve. However, we utilize comparable information in the analytic theory, by diagnosing the time evolving western boundary layer thickness at both ends of the domain.

1) A possible mechanism for the flux difference at the southern edge of the domain

Utilizing the western boundary layer thickness from the numerical model, as above, we can accurately represent the meridional transport at both the southern and northern boundaries using Equations (21) and (22). The regional upper ocean thickness is strongly dependent on these meridional fluxes, especially at the southern boundary where the meltwater flows into the analytic domain. In particular, there are larger northward fluxes at the southern boundary of the analytic domain ($T_{S,i}(t)$) in a top-layer perturbation experiment compared to a bottom-layer perturbation experiment.

We note that this difference in fluxes is also in agreement with the difference in long baroclinic Rossby wave speeds that we found in Equations (12) and (13). The majority of the northward transport out of the input region occurs in the western boundary current, which is generated by the reflection of long Rossby waves as short Rossby waves which dissipate in the boundary region (Pedlosky 1965). Thus, the western boundary current transport in each layer should be consistent with the layer-wise differences in Rossby wave speeds derived in Section 3b. This reflection mechanism is valid at all latitudes (e.g., see Marshall and Johnson 2013), although we draw attention to it here at the southern boundary, to build intuition regarding the $T_{S,i}(t)$ terms.

e. Summary of theory for the dependence of adjustment on meltwater injection depth

The theory derived throughout Section 3 suggests that variations in the regional adjustment of volume anomalies in each density layer are due to layer-wise differences in long baroclinic Rossby wave speeds. Initially, the eastern boundary adjusts due to transport north out of the volume input region in a western boundary current which then travels to the eastern boundary as an equatorial Kelvin wave. The magnitude of the volume transport in the western boundary current is inherently linked to the Rossby wave propagation speed, leading to more transport into the analytic domain in top-layer perturbation experiments. Then, the volume anomaly is propagated into the interior through long baroclinic Rossby waves off the eastern boundary and this occurs more quickly in a top-layer perturbation experiment.

The adjustment of the layer thicknesses in the interior of the basin through the Rossby wave mechanism is visible in maps of the layer thicknesses in the analytic domain 75 years after the volume input begins (Figures 4 and 5). The behavior of the numerical model is approximately captured by the theory presented in Section 3, as can be seen by comparing the maps corresponding to the analytic and numerical results. There is latitudinal dependence of the adjustment due to faster long baroclinic Rossby wave speeds at lower latitudes (see the definitions of $\lambda_1(y)$ and $\lambda_2(y)$). The larger h_1 thicknesses in the top-layer perturbation experiment (Figure 4) than h_2 in the bottom-layer perturbation experiment (Figure 5) is consistent with the faster baroclinic Rossby waves in the top layer than the bottom layer. This difference in the adjustment of each layer explains the difference in the timeseries of the Northern Hemisphere upper ocean thickness anomaly originally shown in Figure 3b and c.

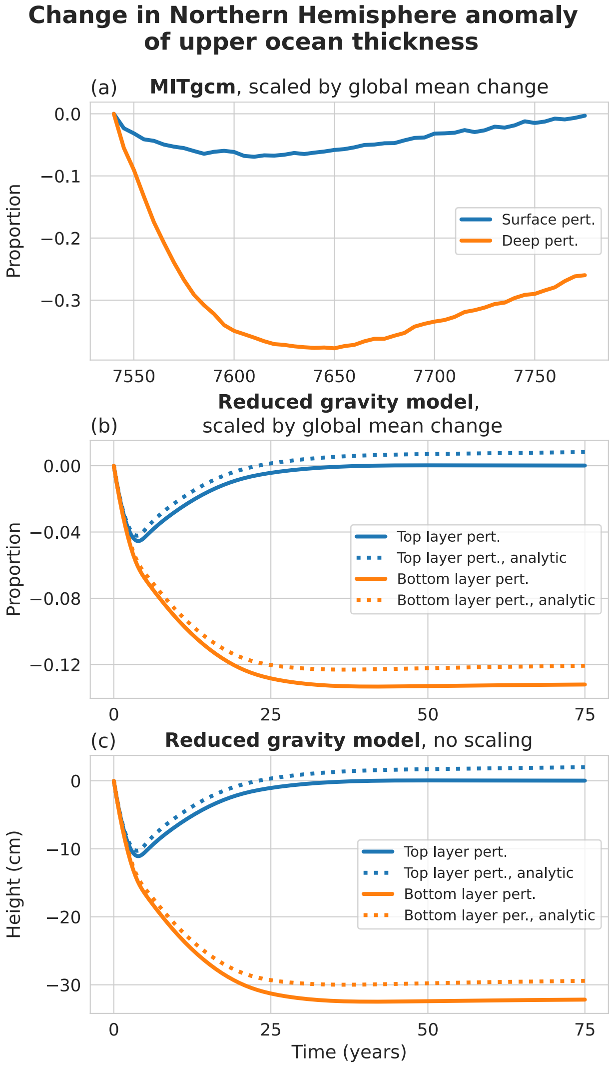

Fig. 3. Timeseries of Northern Hemisphere (NH) response to surface and deep meltwater perturbations. (a): upper ocean thickness in MITgcm run at 1° resolution in an idealized single basin domain, with surface or deep meltwater perturbations at the southern boundary (as in Eisenman et al. 2024). Here, upper ocean thickness is the amount of volume above a bounding isopycnal (as described in text). We plot the NH mean minus the global mean and scale it by the global mean change at year 110, which is approximately when the change in the system first equilibrates. The metric is smoothed with a 5-year moving average. (b): upper ocean thickness ($h_1 + h_2$) in the 2.5-layer reduced gravity model (Section 2a), including numerical (solid lines) and analytic solutions (dotted lines, see Section 3). We plot the NH mean minus the global mean and scale it by the global mean change at year 41, which is approximately when the change in the system first equilibrates. We focus on top or bottom layer perturbations, which is conceptually equivalent to surface or deep perturbations in MITgcm. (c): as panel (b), but without scaling by the global mean change; thus, this is simply the NH mean minus the global mean of $h_1 + h_2$. Note that the horizontal axis ranges are different between panel (a) and panels (b)/(c) due to faster response timescales in the simplified model. A comparable plot for panel (a) in the Southern Hemisphere would be equal and opposite; the same is true for panels (b)/(c), *if* one used the whole numerical domain for averaging.

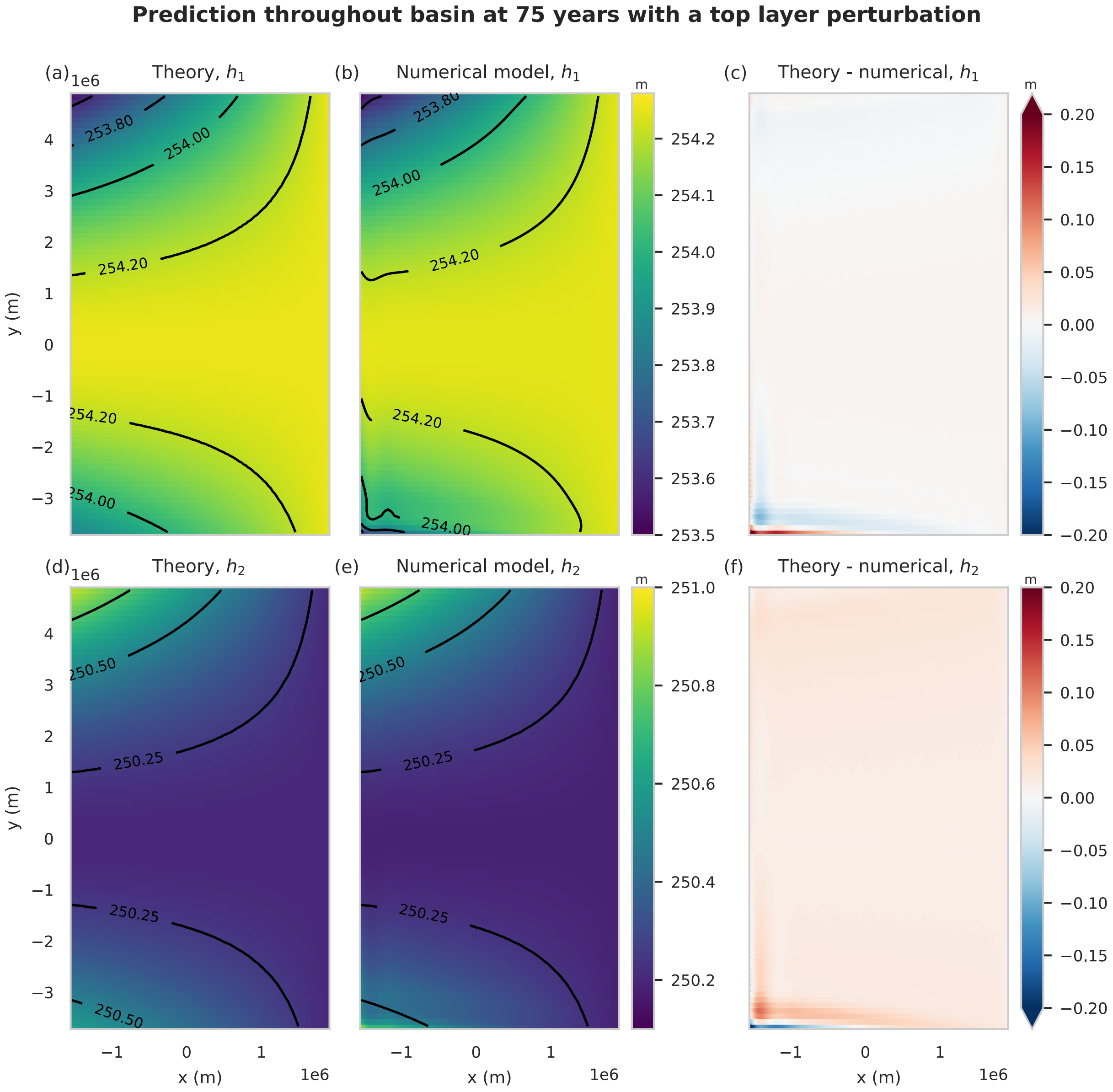

FIG. 4. **Top** layer perturbation experiment comparisons of layer thicknesses (beginning from a resting ocean) between the analytical theory and 2.5-layer numerical model. Here, we utilize $g'_1 = g'_2 = g\frac{2}{1026}$ and $H_1 = H_2 =$ 250m. The region plotted is the analytic domain in Figure 2 (purple). Note that as shown on Figure 2, the analytic region crops out the western boundary current region to better see the adjustment of the interior of the basin. The left column, (a) and (d), shows the predicted layer thicknesses from analytic theory. The middle column, (b) and (e), shows the layer thicknesses from the numerical model. The right column, (c) and (f), shows the difference between the analytic prediction and the numerical model. The top row, (a), (b), and (c), shows quantities for the top layer height h_1 while the bottom row, (d), (e), and (f), shows the corresponding quantities for the bottom layer height h_2.

Accepted for publication in *Journal of Physical Oceanography*. DOI 10.1175/JPO-D-24-0153.1

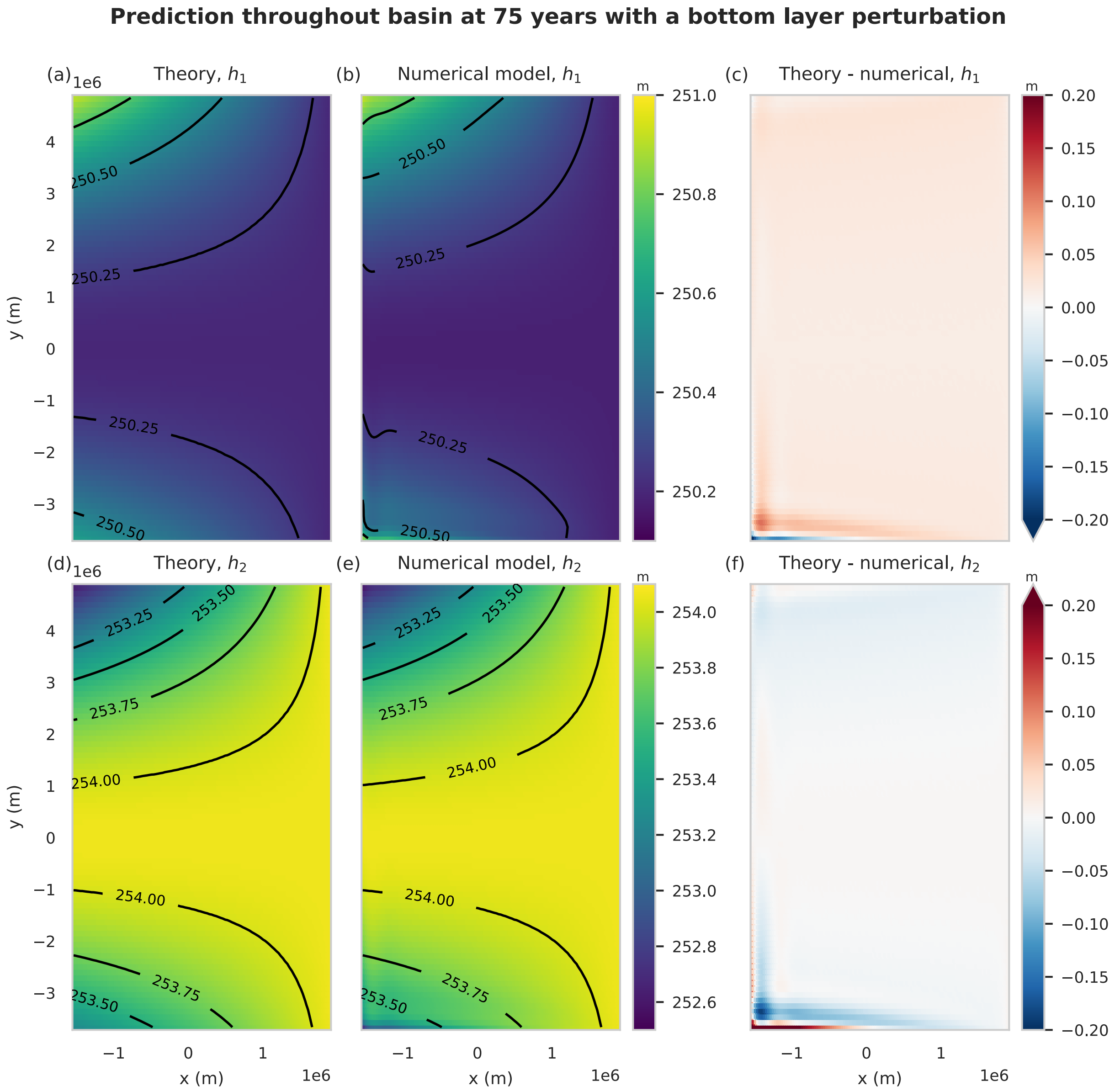

FIG. 5. As in Figure 4 but for a **bottom** layer perturbation experiment.

Accepted for publication in *Journal of Physical Oceanography*. DOI 10.1175/JPO-D-24-0153.1

4. Sensitivity to parameters and unresolved processes

In this section, we explore the sensitivity of the results to (a) parameter choices such as layer thicknesses and stratification and (b) an idealized representation of background transport induced by wind. We comment on the extent to which the perturbed transport, for which we have developed a theory, may help explain the upper ocean adjustment in more complex models.

a. Layer thickness and stratification parameter choices

Faster adjustment of volume perturbations input into the top layer than the bottom layer holds regardless of the choices of initial active layer thicknesses or stratification. However, different quantitative responses in each layer can be achieved by changing these values, because the long baroclinic Rossby wave speeds ($\lambda_1(y)$ and $\lambda_2(y)$) depend on H_1, H_2, g'_1, and g'_2.

1) CASE WHERE $H_1 = H_2$ AND $g'_1 = g'_2$

Here, we examine the case where the initial layer thicknesses of each active layer are the same ($H \equiv H_1 = H_2$) and the density differences between each layer are the same such that $g' \equiv g'_1 = g'_2$. The propagation of anomalies throughout the basin is faster for both layers with either larger layer thicknesses H or density difference g', as expected from $\lambda_1(y)$ and $\lambda_2(y)$, which governs the evolution of the interior upper ocean volume (Equations (12) and (13)). As before, we evaluate the difference in the adjustment timescales by examining the adjustment at the opposite end of the basin from the meltwater input, indicated by the Northern Hemisphere upper ocean thickness anomaly timeseries shown in the three set-ups in Figure 6. Compared to the parameter set-up of $H = 250\text{m}$ and $g' = g\frac{2}{1026}$ (used in Figures 3b/c, 4, and 5), the adjustment of both layers is faster for $H = 250\text{m}$ and $g' = g\frac{3}{1026}$ (dashed) and slower for $H = 100\text{m}$ and $g' = g\frac{2}{1026}$ (dash-dotted).

2) CASE WHERE $g'_1 \neq g'_2$

The stratification in the upper ocean is not generally uniform; thus, parameter choices in our model closer to a realistic stratification would require $g'_1 > g'_2$. This choice leads to a larger difference in the speed of adjustment between the two depths of perturbation, leading to a larger difference in the Northern Hemisphere upper ocean thickness anomaly than for equal reduced gravities (Figure 7a). This can be understood using Equations (D6) and (D7), where we derive

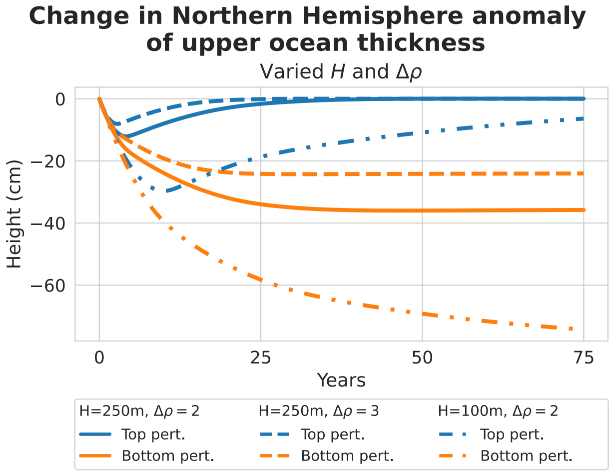

FIG. 6. Numerical 2.5-layer model Northern Hemisphere upper ocean thickness anomaly for simulations with an ocean initially at rest and $H \equiv H_1 = H_2$ and $g' \equiv g\frac{\Delta\rho}{\rho_0} \equiv g'_1 = g'_2$, with a range of H and g' choices (see legend). The solid lines shown here are equivalent to the standard parameter set-up explored in this paper (i.e., that used in Figure 3b/c). It holds that the adjustment in each layer is slower due to either smaller H or smaller g'. A comparable plot for the Southern Hemisphere would be equal and opposite.

analogues to Equations (12) and (13) without assuming $g'_1 = g'_2$ and $H_1 = H_2$. Here, we see that with $g'_1 > g'_2$, there are larger coefficients on the fast timescale and smaller coefficients on the slow timescale in the top layer. This is reversed in the lower layer, such that larger coefficients are on the slow timescale. We note that the timescales themselves also change such that the difference in $\lambda_1(y)$ and $\lambda_2(y)$ is also larger when $g'_1 > g'_2$ than when $g'_1 = g'_2$. Thus, the quantitative difference in adjustment timescales, indicated by the Northern Hemisphere upper ocean thickness anomaly, is dependent on parameter choices, which can be understood by the corresponding faster adjustment in the top layer due to baroclinic Rossby wave propagation (see the analytic solution in Figure 7a).

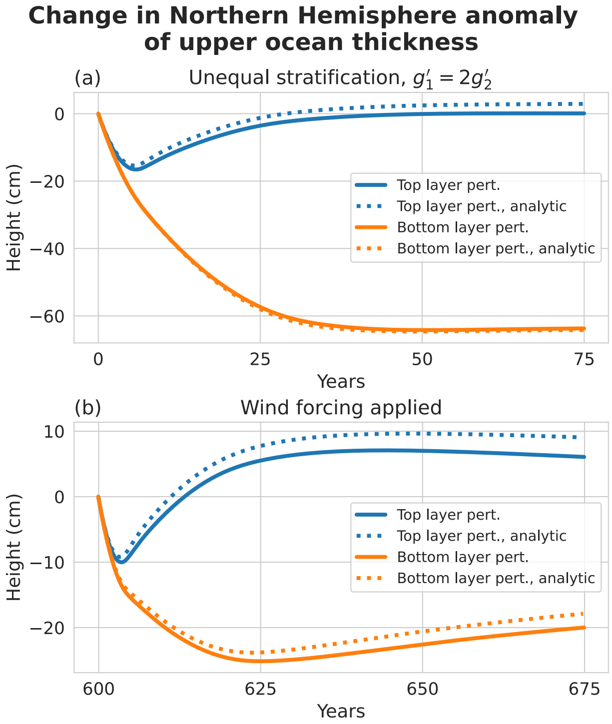

FIG. 7. 2.5-layer model Northern Hemisphere upper ocean thickness anomaly, including numerical and analytical results, for (a) simulations with an ocean initially at rest and $H_1 = H_2 = 250$m and $g'_1 = 2g'_2$ and (b) simulations with wind applied and $H_1 = H_2 = 250$m and $g'_1 = g'_2$. In panel (b), the results are plotted for 75 years of volume input following 600 years of spin-up with wind applied.

b. The effect of wind

The 2.5-layer model, run from a resting state as we've examined thus far, is an idealized representation of processes which propagate the volume anomaly due to perturbed transport induced by the meltwater itself. However, in a more realistic model set-up, we expect the background transport, absent here, will also advect the new meltwater anomaly. For example, we may expect that the Ekman transport driven by wind forcing may advect the anomaly more strongly in the top active layer than the bottom active layer. Here, we use a set-up (see Figure 2a) which approximately mirrors the set-up in MITgcm, where the wind was imposed in a circumpolar current region with a re-entrant channel, and examine the effect of background transport induced by wind in the 2.5-layer model. We note that while the wind forcing in this idealized model is not realistic, especially given that the meltwater input is further north than in the MITgcm model due to the sponge layers, it is sufficient to demonstrate the potential impact of a background transport on the meltwater anomaly. In these runs, we use the same layer thicknesses and reduced gravities as for the results presented in Figure 3b/c. First, we spin-up the ocean for 600 years with an imposed wind forcing, but without a meltwater anomaly. We then create two experiments starting from the end of the control, where meltwater is introduced into either the top or bottom active layer.

Figure 7b shows the Northern Hemisphere upper ocean thickness anomaly in the experiments with wind imposed; here, we have plotted the difference from the end of the spin up run with just wind applied. We find stronger anomalies in both experiments in the Northern Hemisphere compared to the experiments where meltwater is input into a resting ocean due to the additional Ekman transport propagating the anomaly. During the initial adjustment (the first ~ 25 years), the difference between the Northern Hemisphere upper ocean thickness anomaly in each experiment (top- or bottom-layer perturbation) is also slightly larger; this is because the wind more strongly affects transport in the top active layer. This difference reverses after equilibration of the initial response because there is more volume near where the wind is imposed in a bottom-layer experiment due to the initially slower response.

In Figure 7b, we also show the analytic solution, which largely captures the numerical results. Importantly, this analytic solution is possible because the wind is applied south of the analytic domain. Thus, the impact on the analytic domain is only through the $T_{s,1}$ and $T_{s,2}$ terms. If the wind were applied in the interior, the analytic solution would need to be modified to account for Ekman transport, as was done in a 1.5-layer model in Zhai et al. (2014). However, a modification of the analytic solution in the 2.5 layer case would not straightforwardly follow the treatment in Zhai et al. (2014), as the wind would induce a mean flow in both layers, which results in a Doppler shift of the Rossby wave speeds associated with a given mode dependent on the mean flow associated with both layers (e.g., Liu 1999).

We conclude that the adjustment of the volume anomalies throughout the basin will be affected by a background circulation. For example, the effect of wind may account for an additional difference between the dynamic adjustment of volume anomalies in the top layer compared to the bottom layer of the 2.5-layer reduced gravity model during the initial adjustment of the volume anomalies.

5. Conclusion

Antarctica has been losing mass during recent decades (e.g., Otosaka et al. 2023), with additional mass loss projected regardless of emissions scenario over the coming century (e.g., Lowry et al. 2021). Sea level rise from ice sheet mass loss will not be globally uniform, in part due to ocean dynamic processes (e.g., Stammer 2008; Lorbacher et al. 2012; Kopp et al. 2010; Schmidt et al. 2023). Thus, reliable modelling of the ocean's response to meltwater is crucial for predicting the temporal evolution of regional sea level changes. Current projections of sea level rise due to meltwater from ice sheets are typically performed with hosing experiments, where meltwater is input at the surface in an atmosphere-ocean model with a prescribed horizontal distribution and temporal modulation. However, observational evidence suggests that Antarctic meltwater comes primarily from basal melt of ice shelves, and it turbulently mixes as it exits the ice shelf cavity and enters the water column considerably below the surface (Kim et al. 2016; Garabato et al. 2017). Thus, there are important unanswered questions about the sensitivity of regional sea level projections and their evolution in time to the vertical distribution of meltwater input.

In preliminary work, we have demonstrated in an idealized single basin model set-up with MITgcm that the dynamic sea level depends on the depth of meltwater input (Eisenman et al. 2024). In particular, there is more dynamic sea level rise at opposite end of the basin (i.e., in the Northern Hemisphere) and less near the input location (i.e., in the Southern Hemisphere) in response to an idealized Southern Ocean volume input at the surface than at depth. In the present study, we first demonstrated that this result stems from the upper ocean thickness adjustment, which has faster adjustment of the Northern Hemisphere (relative to the global mean) in a surface perturbation experiment than a deep perturbation experiment. Thus, we focused on a 2.5-layer model and presented an associated theory that captures the key dynamics of adjustment in order to interpret the MITgcm results. We have focused on the response of the upper ocean volume transport and how these dynamic processes vary with depth. We have found that the upper ocean volume adjusts faster throughout the basin (indicated by the Northern Hemisphere mean) in response to a top-layer perturbation compared to a bottom-layer perturbation. This is due to the vertical dependence of baroclinic Rossby waves, which determine the response of the signal propagation around the basin on multidecadal (and longer) timescales.

For the theory developed in this paper, we rely on dynamic ocean mechanisms presented in previous studies using reduced gravity models to investigate the response to changes in forcing such as: changes in wind (e.g., Cessi and Otheguy 2003; Zhai et al. 2014), changes in deep water formation (e.g., Kawase 1987; Huang et al. 2000; Johnson and Marshall 2002, 2004; Cessi et al. 2004; Zhai et al. 2011; Nieves and Spall 2018; Sun et al. 2020), and heat sources in the North Atlantic and Southern Ocean (e.g., Hsieh and Bryan 1996). In particular, we assume that there is a fast response from both the western boundary current and Kelvin waves, followed by a slow response governed by Rossby waves emanating off the eastern boundary. This mechanism has also been noted in the response of more complex ocean GCMs to changes in deep water formation (e.g., Goodman 2001; Cessi et al. 2004) or meltwater forcing (Stammer 2008). The key difference between the theory in this paper and previously presented theories for other phenomena that also relied on reduced gravity models is that we investigate the vertical dependence of a volume perturbation by utilizing a second active layer in the model.

While the adjustment mechanism that we identify involving the vertical dependence of baroclinic Rossby waves is expected to play a key role in explaining the baroclinic adjustment of more complex models (e.g., Eisenman et al. 2024), other processes not captured in our idealized theory may also affect the results. In particular, the background circulation, which is driven by wind and buoyancy forcing, will influence the propagation of the volume input. We examined a simplified version of the effect of wind forcing on our result and found that it induces: (1) larger (more positive) volume anomalies at the opposite end of the basin from volume input (Northern Hemisphere) on multidecadal timescales regardless of the depth of perturbation; and (2) a larger difference of the Northern Hemisphere upper ocean thickness anomaly between the surface and deep perturbations during the initial adjustment period. A more realistic inclusion of wind forcing, as well as the inclusion of other processes that are not accounted for here, such as an upper cell meridional overturning circulation, is expected to also influence the response throughout the basin to surface versus deep perturbations on multidecadal timescales. In addition to the background transport in the upper ocean, recent work has demonstrated an expected slowdown of the abyssal overturning due to the shutdown of Antarctic deep water formation driven by ice sheet meltwater (e.g., Lago and England 2019; Li et al. 2023a). As shown explicitly in Lago and England (2019), the change in the abyssal circulation will have an impact on the sea surface height field, largely from the steric signal. In this work, we have assumed the abyss to be motionless and focused only on upper ocean dynamics. Thus, we do not account for this effect or the possible influence of changes in the abyssal cell depending on the depth of meltwater input (visible in Figure S7 of Eisenman et al. 2024). In addition to omitting background transport in both the upper and abyssal ocean, the idealized model presented here may differ from more complex models and real world ocean adjustment because the 2.5-layer model: (1) has different and more simplified stratification than is realistic; (2) is solved on a Cartesian grid rather than in latitude-longitude space; and (3) only properly captures the expected impact of upper ocean dynamic processes, and not the contribution of the abyss (see Appendix B2). However, the theory presented here provides a mechanistic understanding of physical processes which may contribute to the dependence of the time-evolving sea level pattern on meltwater input depth. This dependence may lead to errors in sea level projections that adopt the current standard approach for prescribing meltwater fluxes.

Acknowledgments. This work was supported by NSF OCE grants 2048576 and 2048590. We thank Pavel Perezhogin for helpful discussions on the numerics, as well as David Marshall and an anonymous reviewer for their feedback which helped improve the manuscript. This work was also supported by the New York University IT High Performance Computing resources, services, and staff expertise.

Data availability statement. The code utilized to make all figures in this paper is publicly available at `https://github.com/aurora-bf/2.5_layer_model`. By the time of publication, the code will be associated with a DOI by uploading it to Zenodo. The underlying numerical 2.5-layer model is a significantly modified version of an existing single layer shallow water code (Penn and Vallis 2018); some of the modifications include changing the equations solved and adding a different time-stepping method.

APPENDIX

APPENDIX A

Numerical details for the 2.5-layer model

Numerically, Equations (1) and (2) are solved with finite differences in space on an Arakawa-C grid such that the h_i quantities are located at the center of the cell, the v_i quantities are located at the north and south edges, and the u_i quantities are located at the east and west edges. The equations are integrated in time using the 4th order Runge-Kutta method with a timestep of 250 seconds. The domain is rectangular with size 3.796×10^6 meters in the zonal direction and 1.379×10^7 meters in the meridional direction (see exact dimensions with more significant digits in associated code). We utilize 128 and 129 grid points in the zonal and meridional directions respectively. The domain size was chosen such that the total area is the same as in MITgcm, so that a 0.1 Sv perturbation causes the same global mean volume increase in each model.

We use no-slip and no-normal flow boundary conditions at the edges of the domain to represent solid boundaries. The no-slip condition is implemented using a ghost cell approach (following, e.g., Adcroft and Marshall 1998). We include sponge layers, implemented as a linear drag (Rayleigh friction), at the north and south ends of the domain to damp out gravity waves. Each sponge layer is effective over 18 grid points, with a strength profile that decays exponentially away from the boundary using a decay scale of 5 grid points and a maximum friction coefficient of $r = 10^{-4}\mathrm{s}^{-1}$. In simulations where wind is imposed, a re-entrant channel region is utilized to maintain the flow (see Figure 2b); in the channel region, periodic boundary conditions are used rather than no-slip and no-normal flow conditions.

In the main text, the timeseries in the Northern Hemisphere is calculated using the analytic domain indicated in Figure 2b. Here, in Figure A1, we show a comparable plot to Figure 3c, but over the whole numerical domain; we find that this change only makes a small quantitative difference.

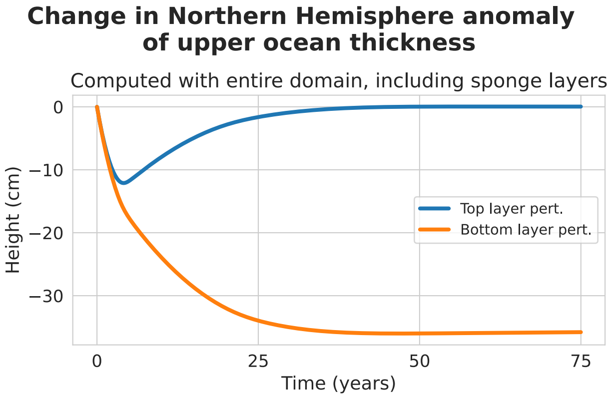

Fig. A1. Numerical 2.5-layer model Northern Hemisphere upper ocean thickness anomaly for simulations with an ocean initially at rest and $H_1 = H_2 = 250$m and $g'_1 = g'_2$. This plot is comparable to the numerical result plotted in Figure 3c, except the whole numerical domain is used when taking the Northern Hemisphere mean. A comparable plot for the Southern Hemisphere would be equal and opposite.

APPENDIX B

Depths of isopycnals in each model

B1. Upper ocean thickness in MITgcm

In Figure B1, we show the zonally averaged depth of the isopycnal chosen to define the upper ocean. Thus, the deepest depth plotted in this figure is equivalent to the upper ocean thickness used

Accepted for publication in *Journal of Physical Oceanography*. DOI 10.1175/JPO-D-24-0153.1

throughout the paper. It is visible that the isopycnal chosen to define the upper ocean correlates to around 1000m in the midlatitudes in the control simulation (panel a).

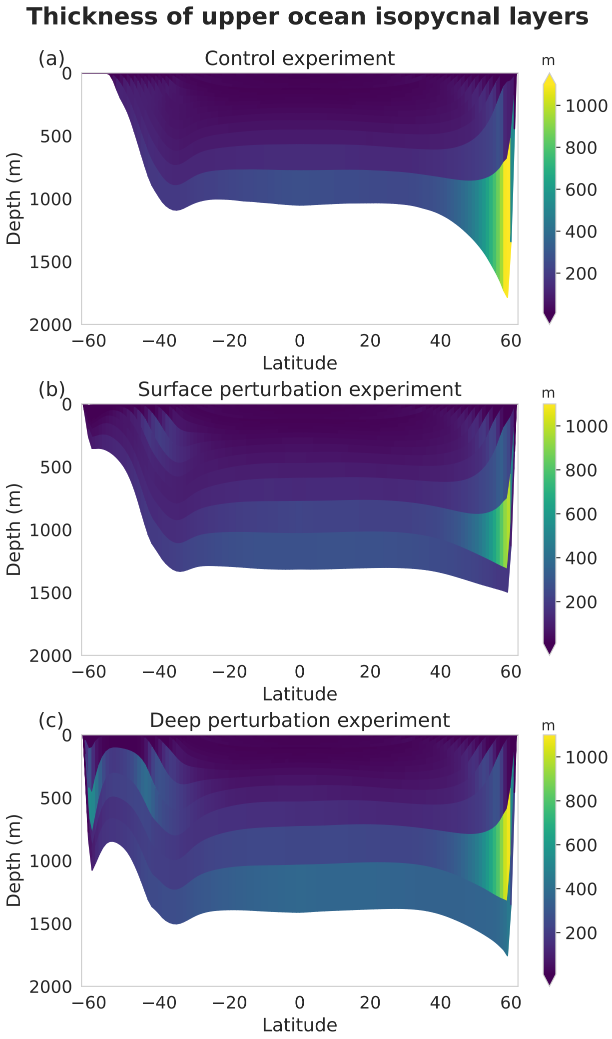

FIG. B1. The thickness of isopycnal layers over the last 50 years of simulation. The layers are plotted in z-space, by projecting the location of the isopycnal back to the appropriate depth using the cumulative sum of the thickness of isopycnal layers above. Here, we plot only the isopycnal layers defined to make up the upper ocean throughout the paper. Thus, the deepest depth of the plotted isopycnals is equivalent to the thickness of the upper ocean (Equation (4)). (a): control experiment, (b): surface perturbation experiment, (c): deep perturbation experiment.

B2. 2.5-layer model sea level

The sea level in the 2.5-layer model can be found by solving for the height of the isopycnal separating the active fluid from the abyssal layer (denoted η_2) and then taking the sea level ζ as $\zeta = \eta_2 + h_2 + h_1$. Using that there is no pressure gradient in the abyss, we find that $\eta_2 = \frac{-\rho_1 h_1 - \rho_2 h_2}{\rho_3} + C(t)$, where $C(t)$ is chosen such that the global mean η_2 relative to the bottom of the stacked fluid is constant in time. We write η_2 as $\eta_2 = < \eta_2 > + \eta_2'$ where $< \eta_2 >$ is prescribed as the global mean height of the abyss (unchanged in time) and η_2' is deviations from this:

$$\eta_2' = \frac{-\rho_1 h_1 - \rho_2 h_2}{\rho_3} - \overline{\frac{-\rho_1 h_1 - \rho_2 h_2}{\rho_3}}. \tag{B1}$$

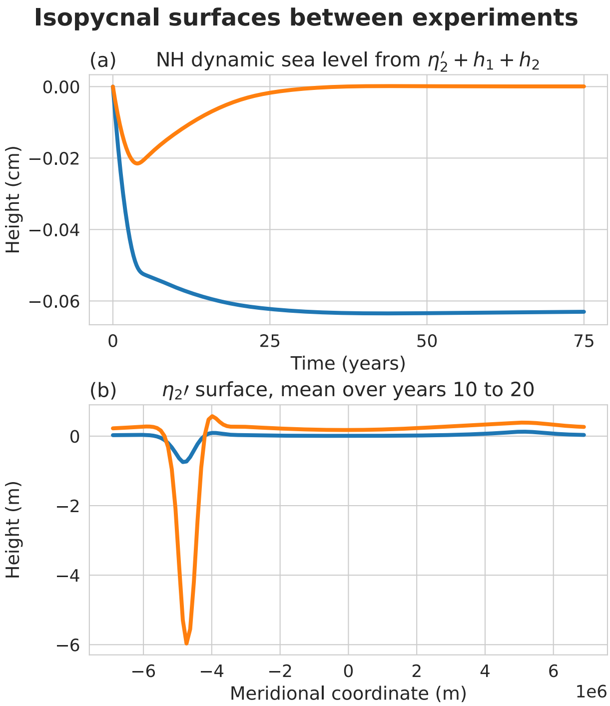

FIG. B2. Isopycnal surfaces in simulations with an ocean initially at rest and $H_1 = H_2 = 250$m and $g_1' = g_2'$. (a): model sea level over time, calculated as $\eta_2' + h_1 + h_2$. This plot is comparable to the numerical result plotted in Figure 3c, except the model sea level is plotted rather than the sum of the active layer thicknesses. (b): the time-mean depth of η_2' from years 10 to 20 plotted against latitude. Thus, this plot can be used to understand the difference in the model free surface compared to the upper ocean thickness focused on in the main text.

We solve for the dynamic sea level using η_2' and the h_1 and h_2 quantities (Figure B2a). This dynamic sea level is equivalent to the steric sea level.

In this paper, we found that the upper ocean transport results in faster propagation of the volume anomalies to the opposite end of the basin (Northern Hemisphere) when inputting volume in the top active layer, but the model sea level shows larger Northern Hemisphere sea level when inputting volume into the bottom active layer. This is because the abyss is motionless and the η_2 isopycnal responds to the weight of the fluid above it. In a bottom-layer perturbation experiment, due to slower propagation of the volume anomalies, more fluid stays in the input region, depressing η_2' more in this location than in a top-layer perturbation experiment. This results in the isopcynal elsewhere becoming more positive due to the requirement of a global mean of 0 (see Figure B2b). Thus, this regional η_2' structure is due to the slower upper ocean transport in a bottom-layer perturbation experiment than a top-layer perturbation experiment. The sum of the regional height of η_2' versus the regional height of $h_1 + h_2$ nearly cancel out as evidenced by the very small values in Figure B2a, but the response of η_2' is slightly more dominant. However, in a more realistic model, the abyss may have its own dynamics, and the spatial structure of the η_2 isopycnal would be set by additional processes, unaccounted for in the 2.5-layer model, including mixing and both the upper and abyssal ocean background state and transport.

Despite the small sea level signal in the 2.5-layer model that does not match the MITgcm sea level, the upper ocean transport investigated in this model is relevant to the MITgcm sea level result because the mechanism of differing speeds of baroclinic Rossby waves with depth is expected to hold and contribute to sea level adjustment. In particular, we demonstrated that the upper ocean thickness adjustment drives the faster adjustment of regional sea level with surface meltwater input (compared to deep meltwater input) in MITgcm.

APPENDIX C

Rossby wave speeds associated with baroclinic modes

The 2.5-layer model has two baroclinic modes (e.g., Vandermeirsch et al. 2003). The potential vorticity in each layer can be modified from the classic 2-layer equations to add the half-layer

Accepted for publication in *Journal of Physical Oceanography*. DOI 10.1175/JPO-D-24-0153.1

dynamics. They are as follows:

$$q_1 = f_0 + \beta y + \nabla^2 \psi_1 + F_1(\psi_2 - \psi_1) \tag{C1}$$

$$q_2 = f_0 + \beta y + \nabla^2 \psi_2 + F_2(\psi_1 - \psi_2) - F_3 \psi_2 \tag{C2}$$

where $F_1 = \frac{f^2}{g_1' H_1}$, $F_2 = \frac{f^2}{g_1' H_2}$, and $F_3 = \frac{f^2}{g_2' H_2}$. Here, we demonstrate the case of equal reduced gravities and mean layer thicknesses, i.e., $F_1 = F_2 = F_3$, which we denote as F.

We make the planar wave assumption ($\psi_i = \tilde{\psi}_i e^{i(kx+ly-\omega t)}$) and set-up the time evolution partial differential equations for q_i:

$$\omega((k^2 + l^2) - F(\tilde{\psi}_2 - \tilde{\psi}_1)) + k\beta\tilde{\psi}_1 = 0 \tag{C3}$$

$$\omega((k^2 + l^2) - F(\tilde{\psi}_1 - \tilde{\psi}_2) + F\tilde{\psi}_2) + k\beta\tilde{\psi}_2 = 0 \tag{C4}$$

We solve an eigenvalue problem based on Equations (C3) and (C4) for Γ such that $\omega((k^2 + l^2) + \Gamma)\tilde{\psi} + \beta k \tilde{\psi} = 0$ where $\tilde{\psi} = [\tilde{\psi}_1, \tilde{\psi}_2]$. Here, Γ is κ_D^2, the inverse of the deformation radius, and $\omega = -\frac{\beta k}{(k^2+l^2)+\Gamma}$.

We find that $\kappa_D^2 = \frac{1}{L_D^2} = \frac{3 \pm \sqrt{5}}{2} F$. We choose the baroclinic modes such that $L_{D,1} > L_{D,2}$ which means $\kappa_{D,1}^2 = \frac{f^2}{g'H}\frac{3-\sqrt{5}}{2}$ and $\kappa_{D,2}^2 = \frac{f^2}{g'H}\frac{3+\sqrt{5}}{2}$.

Thus, using that the long Rossby wave group velocity in the x direction is $c_g^x = \frac{\beta}{\kappa_D^2}$, we find:

$$\begin{aligned} c_{g,1}^x &= \frac{\beta g' H}{f^2} \frac{2}{3 - \sqrt{5}} \\ &= \frac{\beta g' H}{f^2} \frac{3 + \sqrt{5}}{2} \end{aligned} \tag{C5}$$

$$\begin{aligned} c_{g,2}^x &= \frac{\beta g' H}{f^2} \frac{2}{3 + \sqrt{5}} \\ &= \frac{\beta g' H}{f^2} \frac{3 - \sqrt{5}}{2} \end{aligned} \tag{C6}$$

These long Rossby wave speeds are $\lambda_1(y)$ and $\lambda_2(y)$ presented in Section 3b.

APPENDIX D

More details on and extension to the theory

D1. Theory where the heights and reduced gravities are not equal between layers

In Section 3b, we derived an analytic equation that governs transport off the eastern boundary. We assumed that $g'_1 = g'_2$ and $H_1 = H_2$ to simplify interpretation in text. Here, we show an equivalent derivation without this assumption.

The system can be written as in Equation 8, but with

$$\mathbf{A} = \begin{bmatrix} H_1(c_1(y)+c_2(y)) & H_1 c_2(y) \\ H_2 c_2(y) & H_2 c_2(y) \end{bmatrix} \tag{D1}$$

where $c_i(y) = \frac{\beta g'_i}{f^2}$. Dropping y dependences of c_i in the notation, the eigenvalues of the matrix are:

$$\lambda_1(y) = \frac{H_2 c_2 + H_1(c_1+c_2)}{2} + \frac{B}{2} \tag{D2}$$

$$\lambda_2(y) = \frac{H_2 c_2 + H_1(c_1+c_2)}{2} - \frac{B}{2} \tag{D3}$$

where $B = \sqrt{(-H_2 c_2 - H_1(c_1+c_2))^2 - 4H_1 H_2 c_1 c_2}$. We diagonalize with $\mathbf{\Lambda} = \mathbf{P}\mathbf{A}\mathbf{P}^{-1}$ and

$$\mathbf{P} = \frac{H_2 c_2}{B} \begin{bmatrix} 1 & \frac{1}{2} - \frac{H_1(c_1+c_2)}{2H_2 c_2} + \frac{B}{2H_2 c_2} \\ -1 & -\frac{1}{2} + \frac{H_1(c_1+c_2)}{2H_2 c_2} + \frac{B}{2H_2 c_2} \end{bmatrix} \tag{D4}$$

$$= \frac{H_2 c_2}{B} \begin{bmatrix} 1 & F \\ -1 & G \end{bmatrix} \tag{D5}$$

with $F = \frac{1}{2} - \frac{H_1(c_1+c_2)}{2H_2 c_2} + \frac{B}{2H_2 c_2}$ and $G = -\frac{1}{2} + \frac{H_1(c_1+c_2)}{2H_2 c_2} + \frac{B}{2H_2 c_2}$. Using the same process as in Section 3b , we find

$$\begin{aligned} h_1(x,y,t) = {} & \frac{GH_2 c_2}{B} h_1(x_e, t - \tfrac{L_x - x}{\lambda_1(y)}) + \frac{FGH_2 c_2}{B} h_2(x_e, t - \tfrac{L_x - x}{\lambda_1(y)}) \\ & + \frac{FH_2 c_2}{B} h_1(x_e, t - \tfrac{L_x - x}{\lambda_2(y)}) - \frac{FGH_2 c_2}{B} h_2(x_e, t - \tfrac{L_x - x}{\lambda_2(y)}) \end{aligned} \tag{D6}$$

$$\begin{aligned} h_2(x,y,t) = {} & \frac{H_2 c_2}{B} h_1(x_e, t - \tfrac{L_x - x}{\lambda_1(y)}) + \frac{FH_2 c_2}{B} h_2(x_e, t - \tfrac{L_x - x}{\lambda_1(y)}) \\ & - \frac{H_2 c_2}{B} h_1(x_e, t - \tfrac{L_x - x}{\lambda_2(y)}) + \frac{GH_2 c_2}{B} h_2(x_e, t - \tfrac{L_x - x}{\lambda_2(y)}). \end{aligned} \tag{D7}$$

This equation is applied and tested in Section 4a.2.

D2. Additional details to find the eastern boundary heights

In Section 3c, we derive how to find the eastern boundary height in terms of meridional fluxes at the north and south ends of the domain. Here, we explicitly write out the steps between Equation (16) and Equations (17) and (18).

We substitute Equation (16) into Equations (14) and (15):

$$-\frac{\partial}{\partial y}T_1(y,t) = H_1 c_2(y)\left[h_1(x_e,t) - h_1(x_b,y,t) + h_2(x_e,t) - h_2(x_b,y,t)\right] + H_1 c_1(y)\left[h_1(x_e,t) - h_1(x_b,y,t)\right], \tag{D8}$$

$$-\frac{\partial}{\partial y}T_2(y,t) = H_2 c_2(y)\left[h_1(x_e,t) - h_1(x_b,y,t) + h_2(x_e,t) - h_2(x_b,y,t)\right], \tag{D9}$$

to write a volume budget relating the meridional and zonal volume fluxes at each latitude. We write a volume budget for the whole analytic domain by latitudinally integrating Equations (D8) and (D9):

$$h_1(x_e,t)\int_0^{L_y}(c_1(y)+c_2(y))dy + h_2(x_e,t)\int_0^{L_y}c_2(y)dy = \int_0^{L_y}(c_1(y)+c_2(y))h_1(x_b,y,t)dy + \int_0^{L_y}c_2(y)h_2(x_b,y,t)dy + \frac{T_{S,1}(t)}{H_1} - \frac{T_{N,1(t)}}{H_1}, \tag{D10}$$

$$h_1(x_e,t)\int_0^{L_y}c_2(y)dy + h_2(x_e,t)\int_0^{L_y}c_2(y)dy = \int_0^{L_y}c_2(y)h_1(x_b,y,t)dy + \int_0^{L_y}c_2(y)h_2(x_b,y,t)dy + \frac{T_{S,2}(t)}{H_2} - \frac{T_{N,2}(t)}{H_2}, \tag{D11}$$

using $T_{S,i}(t)$ and $T_{N,i}(t)$ as defined in text. The equations that we solve iteratively for the eastern boundary heights (Equation (17) and (18)) are rearrangements of the set of Equations (D10) and (D11).

References

Adcroft, A., and D. Marshall, 1998: How slippery are piecewise-constant coastlines in numerical ocean models? *Tellus A: Dynamic Meteorology and Oceanography*, **50 (1)**, 95–108, https://doi.org/10.3402/TELLUSA.V50I1.14514.

Adusumilli, S., H. A. Fricker, B. Medley, L. Padman, and M. R. Siegfried, 2020: Interannual variations in meltwater input to the Southern Ocean from Antarctic ice shelves. *Nature Geoscience 2020 13:9*, **13 (9)**, 616–620, https://doi.org/10.1038/s41561-020-0616-z, URL https://www.nature.com/articles/s41561-020-0616-z.

Bronselaer, B., M. Winton, S. M. Griffies, W. J. Hurlin, K. B. Rodgers, O. V. Sergienko, R. J. Stouffer, and J. L. Russell, 2018: Change in future climate due to Antarctic meltwater. *Nature*, **564**, 53–58, https://doi.org/10.1038/s41586-018-0712-z.

Cane, M. A., and S. E. Zebiak, 1985: A Theory for El Niño and the Southern Oscillation. *Science*, **228 (4703)**, 1085–1087, https://doi.org/10.1126/SCIENCE.228.4703.1085.

Cessi, P., K. Bryan, and R. Zhang, 2004: Global seiching of thermocline waters between the Atlantic and the Indian-Pacific Ocean Basins. *Geophysical Research Letters*, **31 (4)**, https://doi.org/10.1029/2003GL019091.

Cessi, P., and P. Otheguy, 2003: Oceanic Teleconnections: Remote Response to Decadal Wind Forcing. *Journal of Physical Oceanography*, **33 (8)**, 1604–1617, https://doi.org/10.1175/2400.1.

Chang, P., Y. Fang, R. Saravanan, L. Ji, and H. Seidel, 2006: The cause of the fragile relationship between the Pacific El Niño and the Atlantic Niño. *Nature*, **443**, 324–328, https://doi.org/10.1038/nature05053.

Depoorter, M. A., J. L. Bamber, J. A. Griggs, J. T. M. Lenaerts, S. R. M. Ligtenberg, M. R. Van Den Broeke, and G. Moholdt, 2013: Calving fluxes and basal melt rates of Antarctic ice shelves. *Nature*, **502**, 89–92, https://doi.org/10.1038/nature12567.

Eisenman, I., A. Basinski-Ferris, E. Beer, and L. Zanna, 2024: The Sensitivity of the Spatial Pattern of Sea Level Changes to the Depth of Antarctic Meltwater Fluxes. *Geophysical Research Letters*, **51 (19)**, https://doi.org/10.1029/2024GL110633.

Eyring, V., S. Bony, G. A. Meehl, C. A. Senior, B. Stevens, R. J. Stouffer, and K. E. Taylor, 2016: Overview of the Coupled Model Intercomparison Project Phase 6 (CMIP6) experimental design and organization. *Geoscientific Model Development*, **9 (5)**, 1937–1958, https://doi.org/10.5194/GMD-9-1937-2016.

Farrell, W. E., and J. A. Clark, 1976: On Postglacial Sea Level. *Geophysical Journal International*, **46 (3)**, 647–667, https://doi.org/10.1111/J.1365-246X.1976.TB01252.X.

Garabato, A. C. N., and Coauthors, 2017: Vigorous lateral export of the meltwater outflow from beneath an Antarctic ice shelf. *Nature*, **542**, 219–222, https://doi.org/10.1038/nature20825.

Golledge, N. R., E. D. Keller, N. Gomez, K. A. Naughten, J. Bernales, L. D. Trusel, and T. L. Edwards, 2019: Global environmental consequences of twenty-first-century ice-sheet melt. *Nature*, **566**, 65–72, https://doi.org/10.1038/s41586-019-0889-9.

Goodman, P. J., 2001: Thermohaline Adjustment and Advection in an OGCM. *Journal of Physical Oceanography*, **31 (6)**, 1477–1497, https://doi.org/10.1175/1520-0485(2001)031⟨1477:TAAAIA⟩2.0.CO;2.

Guo, H., Z. Chen, J. Z. Wang, and H. Yang, 2022: Opposite responses of sea level variations to ENSO in the Northwestern Pacific: A transition latitude at 20°N. *Dynamics of Atmospheres and Oceans*, **98**, https://doi.org/10.1016/J.DYNATMOCE.2022.101288.

Hamlington, B. D., and Coauthors, 2020: Understanding of Contemporary Regional Sea-Level Change and the Implications for the Future. *Reviews of Geophysics*, **58 (3)**, https://doi.org/10.1029/2019RG000672.

Hsieh, W. W., and K. Bryan, 1996: Redistribution of sea level rise associated with enhanced greenhouse warming: A simple model study. *Climate Dynamics*, **12 (8)**, 535–544, https://doi.org/10.1007/BF00207937.

Huang, R. X., M. A. Cane, N. Naik, and P. Goodman, 2000: Global adjustment of the thermocline in response to deepwater formation. *Geophysical Research Letters*, **27 (6)**, 759–762, https://doi.org/10.1029/1999GL002365.

Johnson, H. L., and D. P. Marshall, 2002: A Theory for the Surface Atlantic Response to Thermohaline Variability. *Journal of Physical Oceanography*, **32 (4)**, 1121–1132, https://doi.org/10.1175/1520-0485(2002)032⟨1121:ATFTSA⟩2.0.CO;2.

Johnson, H. L., and D. P. Marshall, 2004: Global Teleconnections of Meridional Overturning Circulation Anomalies. *Journal of Physical Oceanography*, **34 (7)**, https://doi.org/10.1175/1520-0485(2004)034⟨1702:GTOMOC⟩2.0.CO;2.

Kawase, M., 1987: Establishment of Deep Ocean Circulation Driven by Deep-Water Production. *Journal of Physical Oceanography*, **17 (12)**, 2294–2317, https://doi.org/10.1175/1520-0485(1987)017⟨2294:EODOCD⟩2.0.CO;2.

Kim, I., D. Hahm, T. S. Rhee, T. W. Kim, C. S. Kim, and S. H. Lee, 2016: The distribution of glacial meltwater in the Amundsen Sea, Antarctica, revealed by dissolved helium and neon. *Journal of Geophysical Research: Oceans*, **121 (3)**, 1654–1666, https://doi.org/10.1002/2015JC011211.

Kopp, R. E., C. C. Hay, C. M. Little, and J. X. Mitrovica, 2015: Geographic Variability of Sea-Level Change. *Current Climate Change Reports*, **1 (3)**, 192–204, https://doi.org/10.1007/S40641-015-0015-5/FIGURES/4.

Kopp, R. E., J. X. Mitrovica, S. M. Griffies, J. Yin, C. C. Hay, and R. J. Stouffer, 2010: The impact of Greenland melt on local sea levels: A partially coupled analysis of dynamic and static equilibrium effects in idealized water-hosing experiments. *Climatic Change*, **103 (3)**, 619–625, https://doi.org/10.1007/S10584-010-9935-1.

Lago, V., and M. H. England, 2019: Projected Slowdown of Antarctic Bottom Water Formation in Response to Amplified Meltwater Contributions. *Journal of Climate*, **32 (19)**, 6319–6335, https://doi.org/10.1175/JCLI-D-18-0622.1.

Li, Q., M. H. England, A. M. Hogg, S. R. Rintoul, and A. K. Morrison, 2023a: Abyssal ocean overturning slowdown and warming driven by Antarctic meltwater. *Nature*, **615**, 841–847, https://doi.org/10.1038/s41586-023-05762-w.

Li, Q., J. Marshall, C. D. Rye, A. Romanou, D. Rind, and M. Kelley, 2023b: Global Climate Impacts of Greenland and Antarctic Meltwater: A Comparative Study. *Journal of Climate*, **36 (11)**, 3571–3590, https://doi.org/10.1175/JCLI-D-22-0433.1.

Liu, Z., 1999: Planetary wave modes in the thermocline: Non-Doppler-shift mode, advective mode and Green mode. *Quarterly Journal of the Royal Meteorological Society*, **125 (556)**, 1315–1339, https://doi.org/10.1002/QJ.1999.49712555611.

Lorbacher, K., S. J. Marsland, J. A. Church, S. M. Griffies, and D. Stammer, 2012: Rapid barotropic sea level rise from ice sheet melting. *Journal of Geophysical Research: Oceans*, **117 (C6)**, https://doi.org/10.1029/2011JC007733.

Lowry, D. P., M. Krapp, N. R. Golledge, and A. Alevropoulos-Borrill, 2021: The influence of emissions scenarios on future Antarctic ice loss is unlikely to emerge this century. *Communications Earth & Environment*, **2 (1)**, https://doi.org/10.1038/s43247-021-00289-2.

Marshall, D. P., and H. L. Johnson, 2013: Propagation of Meridional Circulation Anomalies along Western and Eastern Boundaries. *Journal of Physical Oceanography*, **43 (12)**, 2699–2717, https://doi.org/10.1175/JPO-D-13-0134.1, URL https://journals.ametsoc.org/view/journals/phoc/43/12/jpo-d-13-0134.1.xml.

Mitrovica, J. X., C. C. Hay, R. E. Kopp, C. Harig, and K. Latychev, 2018: Quantifying the Sensitivity of Sea Level Change in Coastal Localities to the Geometry of Polar Ice Mass Flux. *Journal of Climate*, **31 (9)**, 3701–3709, https://doi.org/10.1175/JCLI-D-17-0465.1.

Moorman, R., A. K. Morrison, and A. M. Hogg, 2020: Thermal Responses to Antarctic Ice Shelf Melt in an Eddy-Rich Global Ocean–Sea Ice Model. *Journal of Climate*, **33 (15)**, 6599–6620, https://doi.org/10.1175/JCLI-D-19-0846.1.

Morlighem, M., and Coauthors, 2020: Deep glacial troughs and stabilizing ridges unveiled beneath the margins of the Antarctic ice sheet. *Nature Geoscience*, **13 (2)**, 132–137, https://doi.org/10.1038/s41561-019-0510-8.

Nieves, D., and M. Spall, 2018: Propagation of North Atlantic Deep Water Anomalies. *Journal of Physical Oceanography*, **48 (8)**, 1831–1848, https://doi.org/10.1175/JPO-D-18-0068.1.

Oppenheimer, M., and Coauthors, 2019: Sea Level Rise and Implications for Low-Lying Islands, Coasts and Communities. *IPCC Special Report on the Ocean and Cryosphere in a Changing Climate*, H.-O. Pörtner, D. C. Roberts, V. Masson-Delmotte, P. Zhai, M. Tignor, E. Poloczanska, K. Mintenbeck, A. Alegría, M. Nicolai, A. Okem, J. Petzold, B. Rama, and N. M. Weyer, Eds., Cambridge University Press, 321–445, https://doi.org/10.1017/9781009157964.006.

Otosaka, I. N., and Coauthors, 2023: Mass balance of the Greenland and Antarctic ice sheets from 1992 to 2020. *Earth System Science Data*, **15 (4)**, 1597–1616, https://doi.org/10.5194/ESSD-15-1597-2023.

Park, J. Y., F. Schloesser, A. Timmermann, D. Choudhury, J. Y. Lee, and A. B. Nellikkattil, 2023: Future sea-level projections with a coupled atmosphere-ocean-ice-sheet model. *Nature Communications*, **14**, https://doi.org/10.1038/s41467-023-36051-9.

Pedlosky, J., 1965: A note on the western intensification of the oceanic circulation. *Journal of Marine Research*, **23 (3)**, URL https://elischolar.library.yale.edu/journal_of_marine_research/1055.

Penn, J., and G. K. Vallis, 2018: Linear Shallow Water Model. URL https://empslocal.ex.ac.uk/people/staff/gv219/codes/linearshallowwater.py.

Pritchard, H. D., S. R. M. Ligtenberg, H. A. Fricker, D. G. Vaughan, M. R. Van Den Broeke, and L. Padman, 2012: Antarctic ice-sheet loss driven by basal melting of ice shelves. *Nature*, **484**, 502–505, https://doi.org/10.1038/nature10968.

Rignot, E., S. Jacobs, J. Mouginot, and B. Scheuchl, 2013: Ice-shelf melting around Antarctica. *Science*, **341 (6143)**, 266–270, https://doi.org/10.1126/science.1235798.

Schmidt, G. A., and Coauthors, 2023: Anomalous Meltwater From Ice Sheets and Ice Shelves Is a Historical Forcing. *Geophysical Research Letters*, **50 (24)**, https://doi.org/10.1029/2023GL106530.

Smith, R. S., and Coauthors, 2021: Coupling the U.K. Earth System Model to Dynamic Models of the Greenland and Antarctic Ice Sheets. *Journal of Advances in Modeling Earth Systems*, **13 (10)**, https://doi.org/10.1029/2021MS002520.

Stammer, D., 2008: Response of the global ocean to Greenland and Antarctic ice melting. *Journal of Geophysical Research: Oceans*, **113 (C6)**, https://doi.org/10.1029/2006JC004079.

Sun, S., A. F. Thompson, and I. Eisenman, 2020: Transient Overturning Compensation between Atlantic and Indo-Pacific Basins. *Journal of Physical Oceanography*, **50 (8)**, 2151–2172, https://doi.org/10.1175/JPO-D-20-0060.1.

Swart, N. C., and Coauthors, 2023: The Southern Ocean Freshwater Input from Antarctica (SOFIA) Initiative: scientific objectives and experimental design. *Geoscientific Model Development*, **16 (24)**, 7289–7309, https://doi.org/10.5194/gmd-16-7289-2023.

Taylor, K. E., R. J. Stouffer, and G. A. Meehl, 2012: An Overview of CMIP5 and the Experiment Design. *Bulletin of the American Meteorological Society*, **93 (4)**, 485–498, https://doi.org/10.1175/BAMS-D-11-00094.1.

Todd, A., and Coauthors, 2020: Ocean-Only FAFMIP: Understanding Regional Patterns of Ocean Heat Content and Dynamic Sea Level Change. *Journal of Advances in Modeling Earth Systems*, **12 (8)**, https://doi.org/10.1029/2019MS002027.

Vandermeirsch, F. O., X. J. Carton, and Y. G. Morel, 2003: Interaction between an eddy and a zonal jet: Part II. Two-and-a-half-layer model. *Dynamics of Atmospheres and Oceans*, **36 (4)**, 271–296, https://doi.org/10.1016/S0377-0265(02)00066-0.

Zhai, X., H. L. Johnson, and D. P. Marshall, 2011: A model of Atlantic heat content and sea level change in response to thermohaline forcing. *Journal of Climate*, **24 (21)**, 5619–5632, https://doi.org/10.1175/JCLI-D-10-05007.1.

Zhai, X., H. L. Johnson, and D. P. Marshall, 2014: A Simple Model of the Response of the Atlantic to the North Atlantic Oscillation. *Journal of Climate*, **27 (11)**, 4052–4069, https://doi.org/10.1175/JCLI-D-13-00330.1.